Experiments in Fluids (2020) 61:86
https://doi.org/10.1007/s00348-020-2920-1

RESEARCH ARTICLE

Formation and dynamics of compressible vortex rings generated by a shock tube

Liang Qin[1] · Yang Xiang[2] · Haiyan Lin[1] · Hong Liu[2]

Received: 30 July 2019 / Revised: 15 January 2020 / Accepted: 14 February 2020 / Published online: 2 March 2020

Abstract

Particle image velocimetry experiments were carried out to investigate the formation and dynamics of compressible vortex rings (CVRs) generated by a shock tube apparatus. Five shock Mach numbers (M_s) including $M_s = 1.28$, 1.39, 1.48, 1.56, and 1.59 are designed to generate the three typical CVRs including shock-free CVRs, CVRs with embedded shock, and CVRs with embedded shock and counter-rotating vortex rings (CRVRs). Experimental results show that after the incident shock leaves the tube exit, CVRs roll up, grow in size, and then pinch off at a certain timescale. By referring to the idea of vortex formation time, CVRs are found to pinch off at the dimensionless formation number within the narrow range of $F^* = 3.5 \pm 0.5$ for the range of $M_s = 1.28$–1.59. When $M_s \geq 1.48$, the embedded shock appears inside the CVRs and axially stretches the vortex core, therefore significantly affecting the dynamics of CVRs. The maximum axial velocity along the centerline, the non-dimensional mean core radius, and the propagation velocity of CVRs all increase with M_s when $M_s \leq 1.48$; however, they no longer increase when $M_s > 1.48$ owing to the effects of embedded shock. In addition, the propagation velocity estimated by the formula given by Moore (Proc R Soc Lond A 397:87–97, 1985) shows the better agreement with that obtained by experimental measurement for shock-free CVRs than CVRs with embedded shock and CVRs with CRVRs.

✉ Yang Xiang
xiangyang@sjtu.edu.cn

✉ Hong Liu
hongliu@sjtu.edu.cn

[1] School of Aeronautics and Astronautics, Shanghai Jiao Tong University, Shanghai 200240, China

[2] J.C. Wu Center for Aerodynamics, School of Aeronautics and Astronautics, Shanghai Jiao Tong University, Shanghai 200240, China

Graphic abstract

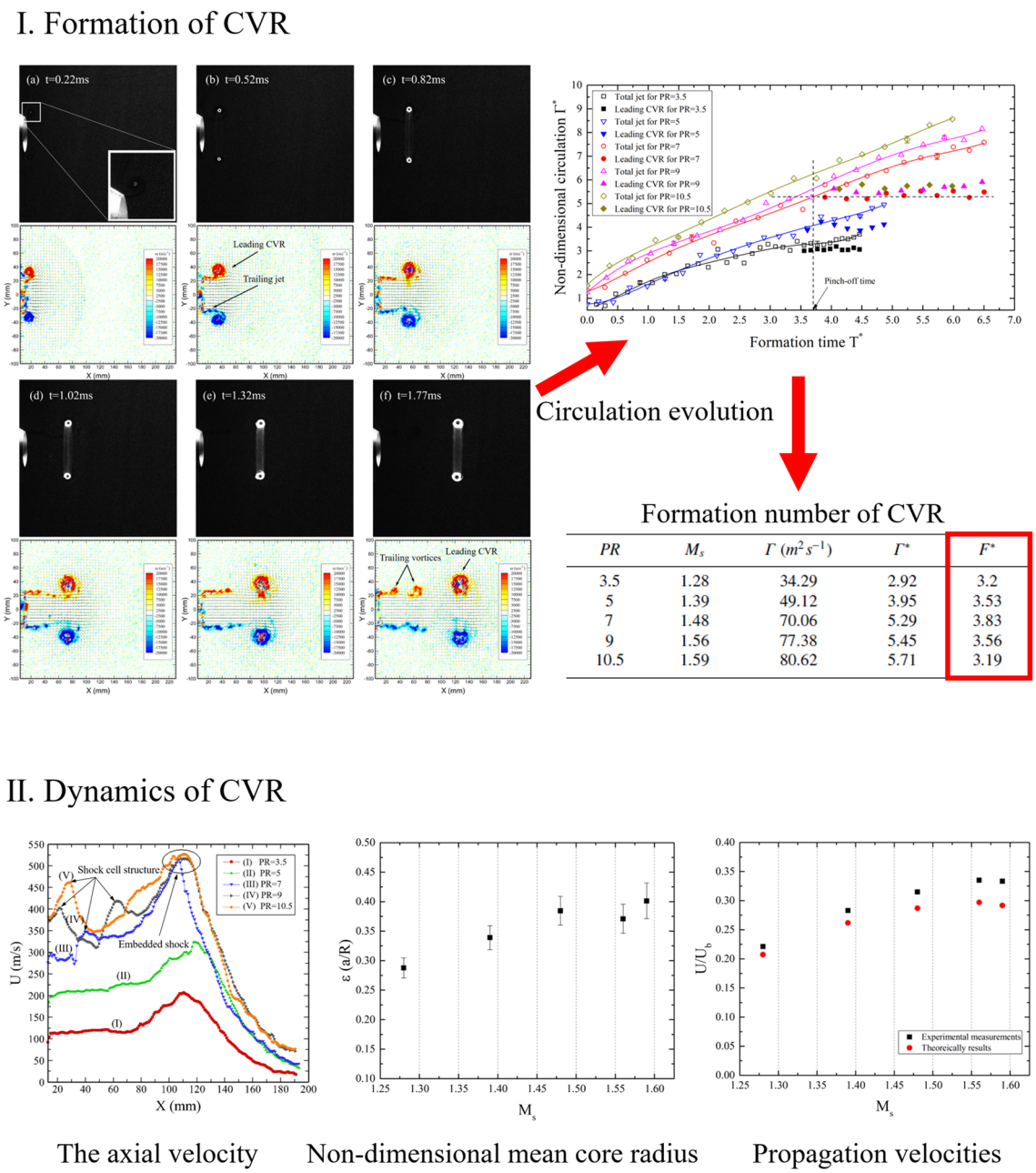

1 Introduction

Vortex rings are one of the most fundamental and fascinating structures in three-dimensional flows. In the past several decades, vortex rings have attracted the attention of massive investigators and a great amount of researches has been reported on them (Shariff 1992; Aydemir et al. 2012; Dora et al. 2014). Most of the researches focused on the incompressible vortex rings (ICVRs), which are usually generated by the piston-cylinder apparatus in laboratory (Xiang et al. 2018a, b; Aydemir et al. 2012). As one canonical vortex in compressible flows, compressible vortex rings (CVRs) always appear in the flows from a rocket nozzle, diesel engine exhaust mufflers, and pulse combustors. In addition, CVRs can also be formed from volcanic eruption in nature. Understanding the formation and dynamics

of CVRs is of particular importance to exemplify the other compressible vortices and improve the performance of the industrial systems in engineering. Compared with ICVRs, the formation and dynamics of CVRs are more complex due to the compressibility effects and the emergence of shock/expansion waves.

In the laboratory, a canonical and axisymmetric CVR is generated from a shock tube at the open end with some fascinating phenomena including the process of the shock wave propagation and diffraction expansion, slip stream separation, and vortex sheet rolling-up. The first recorded observation of the propagation of the shock wave along the cylindrical tube was reported by Vieille (1899), who used schlieren technique to find the formation of the incident shock and examined the propagation velocity of shock wave. Then, Payman and Shepherd (1946) studied the motion of the shock wave for different lengths of driver section and different driver gases by using schlieren technique. In the similar manner, Elder and Haas (1952), Phan and Stollery (1983), Baird (1987), and Minota (1997) investigated the structures and characteristics of CVRs generated by an open-end shock tube. Owing to the technical limitations, these investigations are mostly qualitative observations.

Since the late 1990s, the study of CVRs has been carried out to a greater depth due to the rapid advancements in experimental measurement and computational fluid dynamics technology. With these improvements, the detailed information of CVRs can be quantitatively extracted. Particle image velocimetry (PIV) technology was first used by Arakeri et al. (2004) to analyze the formation process of CVRs for three Mach numbers of the incident shock wave (M_s) 1.1, 1.2, and 1.3. They found that the stable propagation velocity of CVRs is approximately $0.7U_b$, where U_b is the velocity at the nozzle just behind the shock. By using PIV, Zare-Behtash et al. (2009) focused on the formation of CVRs with various nozzle geometries. They found that the CVR, which generated from the square

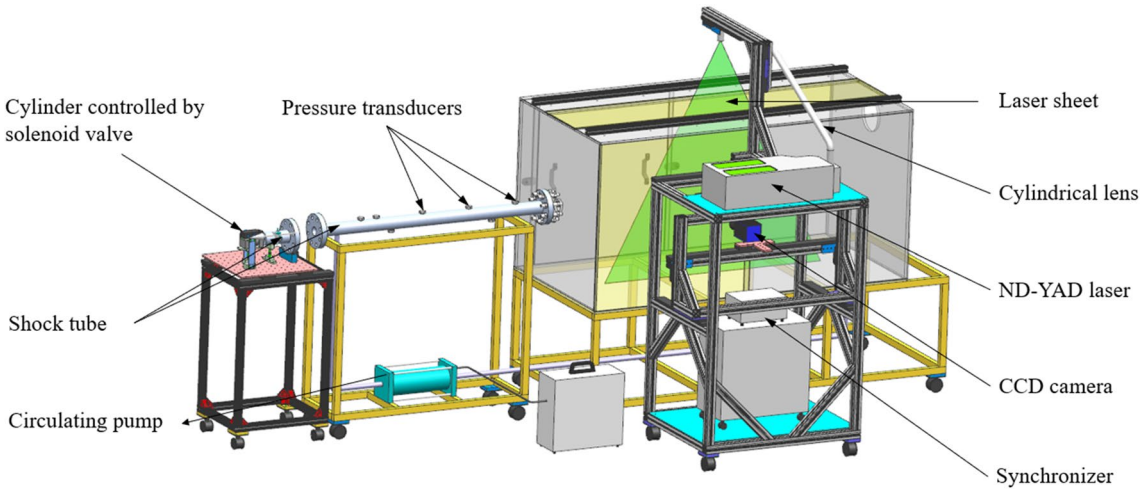

Fig. 1 Schematic of the experimental setup with a shock tube apparatus

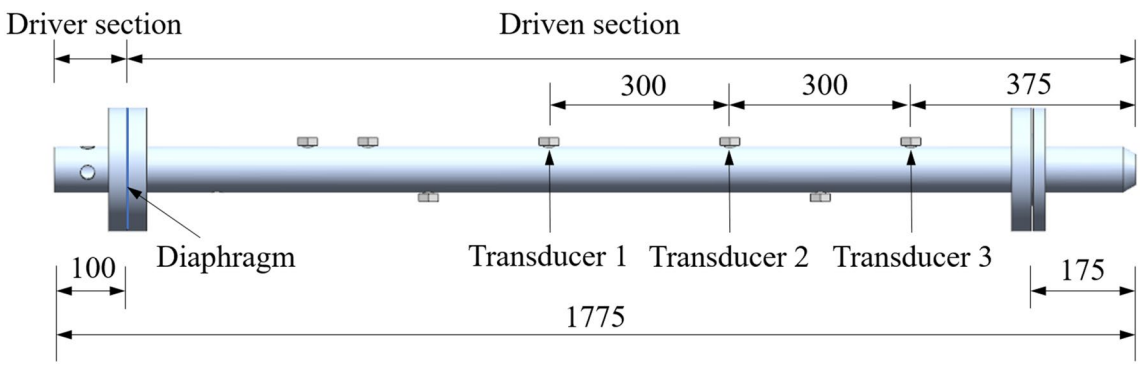

Fig. 2 Geometric parameters of the shock tube

Table 1 Mach number of the shock wave in shock tube

PR	M_s (experimental measurements)	M_s (theoretical results)
3.5	1.28	1.30
5	1.39	1.40
7	1.48	1.50
9	1.56	1.57
10.5	1.59	1.60

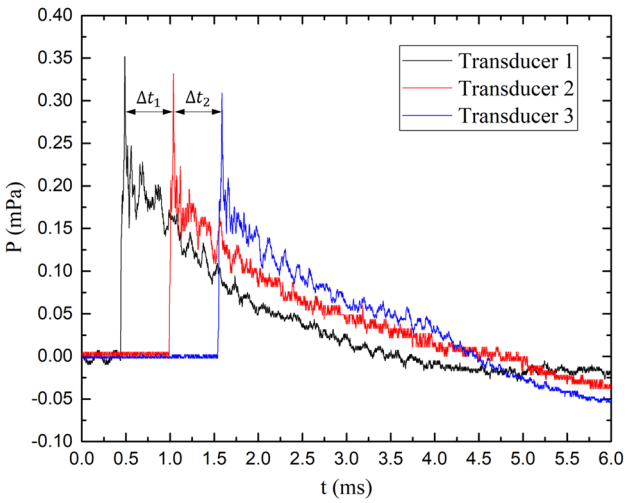

Fig. 3 Pressure transducer signals in the driven section for the case of PR = 10.5

or elliptic nozzle, was proceeding axis switching during the downstream propagation. For the eye-shaped nozzle, the growth rate of CVR diameter weakly depends on the Mach number of shock wave in the early stage, while the circulation of CVR was reduced due to the influence of viscosity in the late stage. As is well known, for the CVRs generated by a shock tube, their characteristics are strongly dependent on two key parameters. One is the pressure ratio between driver section and driven section (PR), and the other one is the length of driver section (DL). In general, PR determines M_s and affects the compressibility of CVRs. Depending on M_s, CVRs mainly exhibit three types. The first type is the shock-free CVR for $M_s < 1.43$, and Elder and Haas (1952) studied the propagation velocity of shock-free CVR for $M_s = 1.12$ and 1.32. The second type is the CVR with embedded shock for $1.43 < M_s < 1.60$. Murugan et al. (2012) studied the formation and evolution of shock cell structure in CVRs by numerical simulation and PIV measurements, and they found that the embedded shock is the major factor on CVR stretching and deformation for $M_s = 1.57$. The last type is the CVR with embedded shock along with counter-rotating vortex rings (CRVRs) ahead of it for $M_s > 1.6$. Brouillette and Hebert (1997) first observed the appearance of CRVRs by using shadowgraphy. Ishii et al. (1999) and Kontis et al. (2006) observed the counter-rotating ahead of primary ring after Brouillette and Hebert, and the exact dynamics of the counter-rotating vortex ring were first reported by Murugan and Das (2007). Then, Murugan and Das (2010), Murugan et al. (2013), and Dora et al. (2014) investigated the formation of CRVRs in detail and their interaction with the CVR. In addition, the numbers of CRVRs are found to be dependent on PR, as well as DL. In 2014, Dora et al. (2014) found that the formation of CRVRs is largely owing to the Kelvin–Helmholtz-type shear flow instability of the slipstream originating from the triple point of the Mach disk. These investigations have provided plentiful knowledge on the formation and flow pattern of CVRs generated by a shock tube; however, the knowledge of the dynamics of CVRs is greatly lacking.

In addition to the experimental and numerical investigations, some theoretical analyses were performed to study the compressibility effects on the dynamics of compressible vortex including the CVR. Based on the mathematic solutions for a vortex, Moore (1985) proposed a theoretical formula for estimating the propagation velocity of an inviscid CVR with calorically perfect gas. It is found that the propagation velocity of CVRs should be slowed down due to the compressibility effects. Similarly, compressibility has major impact on the structure of vortex by some other researchers. Applying the solution of the Euler equation to the compressible flow fluid, Brown (1965) examined the effect of compressibility on the inviscid leading-edge vortex and illustrated that compressibility mainly acts near the axis which called boundary-layer effect. Using a perturbation method in theoretical calculation, Moore and Pullin (1987) discussed the motion of a vortex pair in an inviscid compressible fluid. For given dimensions and circulation, they found that the distortion of the vortex pair boundary increased due to compressibility effects. Although it is undoubted that the compressibility effects play a significant role on the features of compressible vortices, to the best of our knowledge, the dynamics of CVRs with a wide range of M_s are rarely investigated.

Compared with CVRs, the dynamics of ICVRs have been widely investigated. Fraenkel (1972) proposed second-order formula to describe the ICVRs that have finite but thin core. Subsequently, some modifications for the ICVR dynamics were given by Sullivan et al. (2008) and validated by comparing with the experimental results. For the ICVRs generated by a piston-cylinder apparatus, the vorticity in their core satisfies Gaussian distribution, their circulation formation can be predicted by the Slug model, and their propagation velocity depends on the Biot–Savart

law (Didden 1979; Krueger 2005; Shaffman 1970). In addition, a vortex pinch-off process was observed in the formation of ICVRs by Gharib et al. (1998) and suggests an optimal vortex formation principle (Dabiri 2009). After the occurrence of pinch-off, ICVRs cannot grow any longer and the additional vorticity rolls up to form the secondary trailing vortices (Gao and Yu 2012). Based on the dynamics of ICVRs, an analytical model was proposed by Gao and Yu (2010) to describe the formation and pinch-off of ICVRs. However, the pinch-off of CVRs generated by a shock tube has not been identified. Therefore, the knowledge of ICVRs can provide important reference to understand the formation and dynamics of CVRs.

In sum, this paper attempts to analyze the formation of the CVRs generated by a shock tube and investigate the compressibility effects on the dynamics of CVRs. A shock tube apparatus is designed to generate CVRs and PIV technique is used to measure the time-dependent flow fields during CVR formation. Based on PIV measurements, the flow patterns are shown to explain the formation of CVRs and the development of some inner structures. Subsequently, the circulation production and vortex pinch-off phenomena are investigated in detail. To investigate the compressibility effects on the dynamics of CVRs, the core size, vortex radius, and propagation velocity are analyzed. In the present study, the types of CVRs include the shock-free CVRs, CVRs with embedded shocks, and CVRs with CRVRs and embedded shocks.

2 Experimental setup and techniques

An open-end shock tube apparatus is used to obtain the axisymmetric CVRs, as shown in Fig. 1. Our experimental setup mainly includes a shock tube apparatus to generate CVRs, the PIV measurement system to measure the flow field of CVRs, three pressure transducers to measure the strength of incident shock, and a synchronically trigger system to control the operation of laser and camera.

The geometries of the shock tube are shown in Fig. 2, which consists of a driver section and a driven section. The driver section is filled with compressed air. Both the driven section and box are opened to share the same condition with the atmosphere. The experimental temperature is 25 ± 1 °C. In order to investigate the compressibility effects on the CVR formation and dynamics, the driver section was fixed with the constant length of 100 mm and the pressure ratio between driver section and driven section (PR) was changed. The shock tube had an inner diameter (D_t) of 52 mm and a wall thickness of 12 mm. The driven section had a wedge-shaped edge of 30° at the end to ensure the smooth rolling-up of the vortex sheet at the exit. A cylinder was mounted on the other side of the driver section, which was controlled by solenoid valve and driven by compressed air. Mylar sheets of different thicknesses were used as diaphragms and were entirely ruptured using an ejector pin, which was driven by the piston of cylinder. In our study, the thickness of diaphragms was 0.038 mm, 0.05 mm, 0.08 mm, 0.1 mm, and 0.12 mm corresponding to PR = 3.5, PR = 5, PR = 7, PR = 9, and PR = 10.5. The driver section was equipped with a manometer (Omega DPGM409-035BA) used to monitor air pressure.

The pressure measurement system was used to measure the strength of the shock wave by calculating the propagation velocity of the shock wave with the three pressure transducers (PCB 113B21). The variations of the pressure signals recorded by the three transducers are shown in Fig. 3. The shock wave Mach number (M_s) at different PR values can be calculated by measuring the time intervals Δt_1 and Δt_2 between the two transducers. From the results, we can find that the propagation velocity of the shock wave for PR = 10.5 in the shock tube is reduced from 540.15 to 537.28 m/s. The propagation velocity of the shock wave is decreased by less than 1% along the shock tube. Moreover, due to the short driver section used in the present experiments, strong pressure fluctuations and significant pressure attenuation are observed in Fig. 3, thereby indicating that the shock pressure profile is unsteady and the shock in the shock tube is more similar to a blast wave (Chandra et al. 2012; Murugan and Das 2018). In this paper, the Mach number of this shock wave is taken as the average of the two segments. In addition, the Mach number of shock wave can be calculated theoretically by

$$\mathrm{PR} = \left[1 + \frac{2\gamma}{\gamma+1}\left(M_s^2 - 1\right)\right] \times \left[\frac{1}{1 - [(\gamma-1)(\gamma+1)]\left(M_s - 1/M_s\right)}\right]^{2\gamma/(\gamma-1)} \quad (1)$$

where γ is the thermodynamic coefficient of air.

In Table 1, the Mach numbers of shock wave obtained by experimental measurements and theoretical calculations are shown. It is found that the experimental results are up to approximately 1.5% smaller than theoretical results. This slight difference is largely attributed to the influence of viscous boundary layer, the impact of the diaphragm breaking process, and the short driver section.

The velocity field was measured by a PIV system, which consists of a double-pulsed Nd:YAG (380 mJ/pulse) laser for illumination, a 14-bit PCO.2000 CCD camera for capturing the particle images, and a synchronization (DG645). The $C_{26}H_{50}O_4$ oil is evaporated as the tracing particles that are seeded by a LAVSION generator. The average size of the oil mist particles was approximately 0.2–0.5 µm, and the

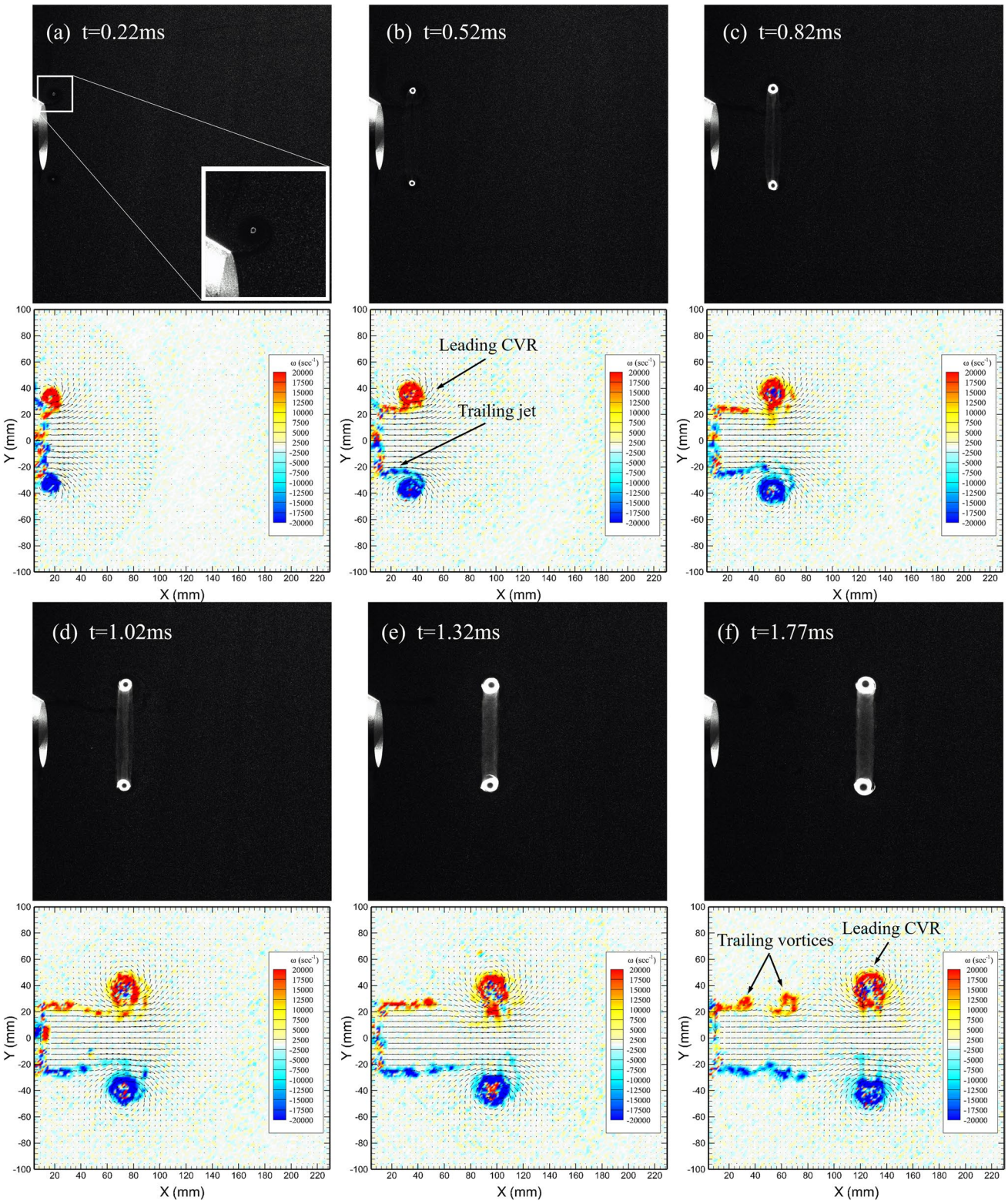

Fig. 4 Flow visualization and the corresponding velocity vector superimposed with vorticity contour for the case of PR = 3.5 at some instants: **a** $t = 0.22$ ms, **b** $t = 0.52$ ms, **c** $t = 0.82$ ms, **d** $t = 1.02$ ms, **e** $t = 1.32$ ms, and **f** $t = 1.77$ ms

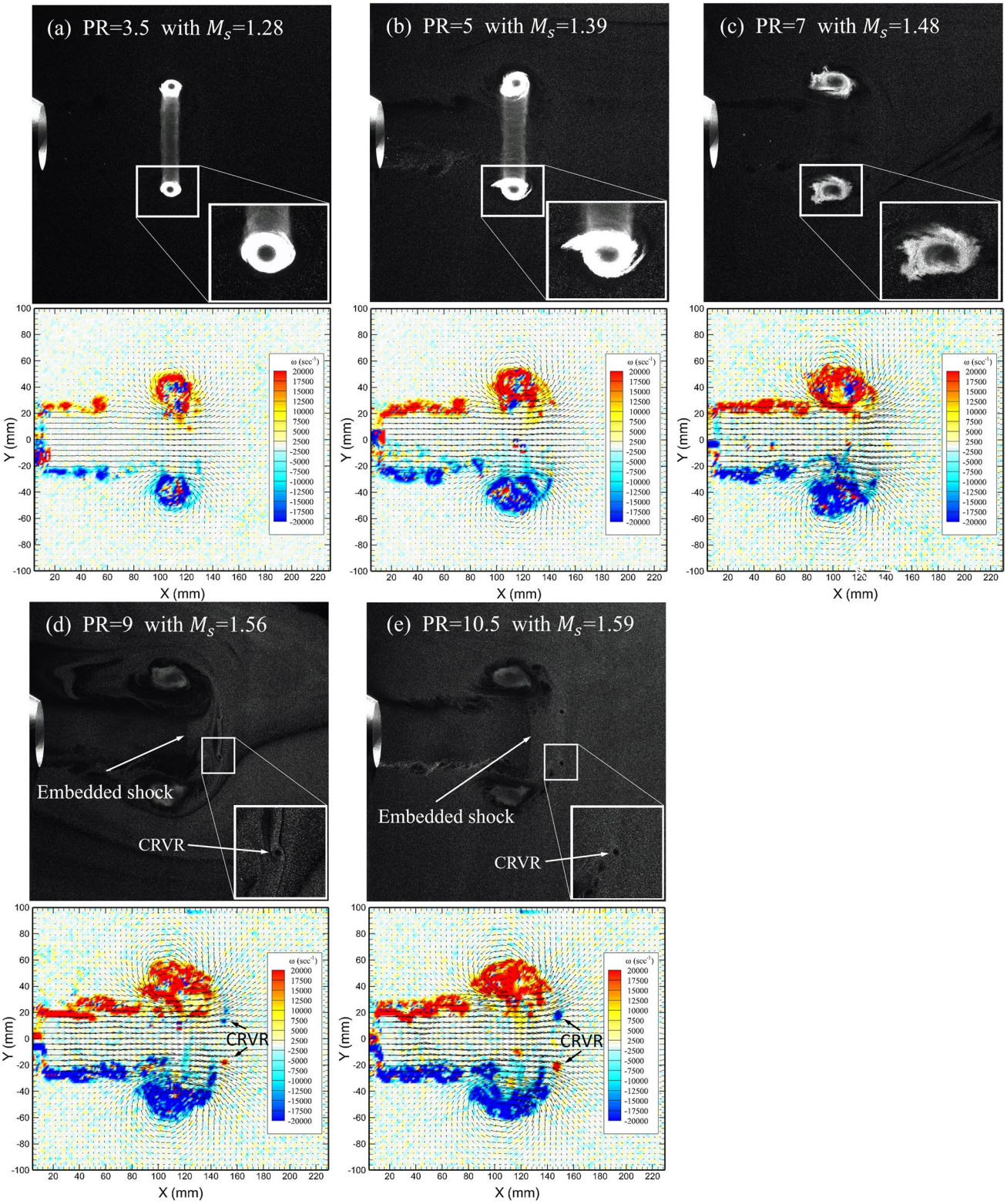

Fig. 5 Particle images and the corresponding velocity vectors superimposed with vorticity contour for the CVRs propagating at the same position. **a** PR = 3.5 at t = 1.37 ms, **b** PR = 5 at t = 0.99 ms, **c** *PR*=7 at t = 0.69 ms, **d** *PR*=9 at t = 0.73 ms, and **e** PR = 10.5 at t = 0.72 ms

followability is good enough to capture details of the flow field. The steps of filling particles are as follows: (1) after the driver section and the driven section are connected, the tracing particles are seeded into the driven section and the box; (2) the circulating pump is able to get the particles into the driven section; and (3) waiting for a while to make the particles more uniform and the experiment can be started. A cylindrical lens was used to obtain a 2-mm thin laser sheet, which was placed perpendicular to the exit plane of shock tube and passed the centerline. Perpendicular to the laser sheet, a high-resolution camera with 2048 × 2048 pixels was placed to record the flow fields. The timing between the two pulsed laser pulses was set to be 3–5 μs based on the shock wave velocity inside the shock tube. The paired images recorded by the camera were processed by a commercial PIV software (TSI Insight 4G). The interrogation zones were 32 × 32 pixels with 50% overlap. After processing, the flow fields of 164 × 164 velocity vectors on the interrogation area of 236 mm × 236 mm were constructed. A second-order accurate scheme was employed to calculate the vorticity fields with the finite differences in the velocity data with eight neighboring points.

Here, it should be mentioned that in the box, the tracing particles are filled uniformly. The size of the box is designed by 2030 mm in length, 1000 mm in width and 1000 mm in height, which is large enough to ensure that the reflected shocks have no influence on the CVR in the time period we care about. And the schlieren technique is used to prove that the reflected shocks have not influenced on the formation of CVR in our study. To record the flow fields at a given time, the signal of pressure transducer (labeled 3) is used as a trigger to control the laser and CCD camera to operate simultaneously with the synchronization. By varying the delay in the synchronizing system, we can obtain the flow field at different given moments. In our study, the measurement of propagation velocity of the shock wave for each PR was repeated 40 times, and the experimental results showed good repeatability. ($\Delta M_s/M_s < 1\%$, where ΔM_s represents the maximal discrepancy of Mach number of the shock between these runs.) In order to satisfy the constraints, such as perfect position between laser sheet, camera and calibration plate, particle concentration and followability, data postprocessing of the PIV measurement system, the uncertainty in the velocity of the flow field is within 1% as mentioned by Dora et al. (2014).

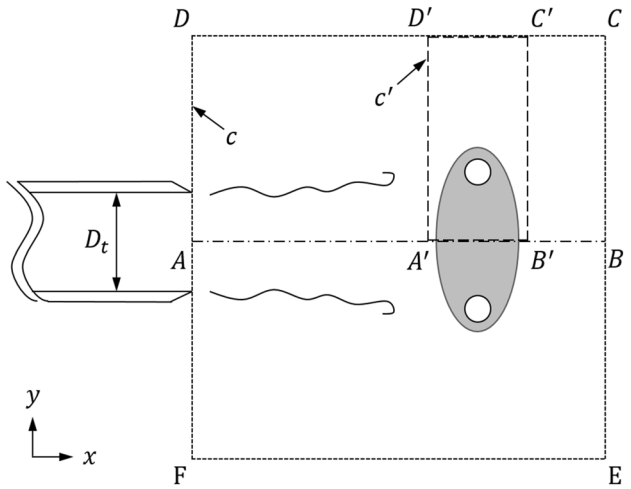

Fig. 6 Circuit for calculating circulation

3 Results and discussion

3.1 Flow visualization of CVR formation and flow pattern

Through precisely controlling the triggering time to operate the PIV system, we obtained a series of time-dependent flow fields of CVRs. The flow patterns of CVRs for PR = 3.5 with M_s= 1.28 at t = 0.22 ms, t = 0.52 ms, t = 0.82 ms, t = 1.02 ms, t = 1.32 ms, and t = 1.77 ms are shown in Fig. 4a–f. In the present study, the initial time t = 0 ms is set to be the time when the incident shock arrives at the exit plane of the shock tube. In Fig. 4, the upper picture is the flow visualization images and the lower one is the corresponding velocity vector superimposed with vorticity contour. From the flow visualization images, we can see that few particles can stay in the center of the vortex core of CVR due to the strong centrifugal force, and the particles mainly accumulate in the boundary region of the vortex core. This phenomenon was also observed by Arakeri et al. (2004) and Murugan and Das (2010); Murugan et al. (2012) as well.

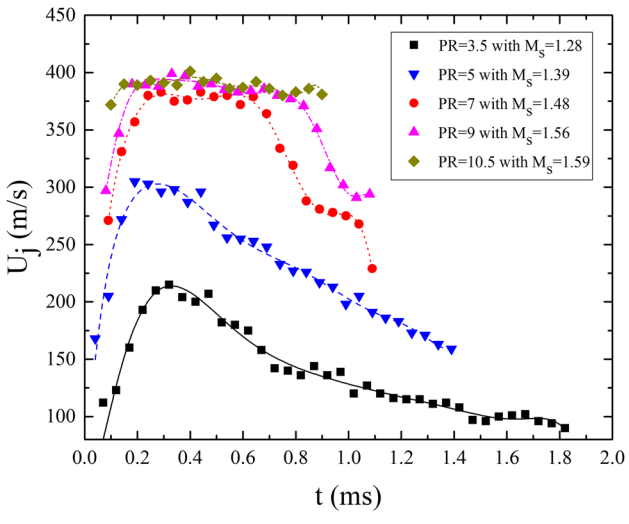

Fig. 7 The velocity of the fluid at the nozzle of the shock tube for the five cases

Table 2 Circulation of the leading CVR and its corresponding formation number for each case

PR	M_s	Γ (m^2s^{-1})	Γ^*	F^*
3.5	1.28	34.29	2.92	3.2
5	1.39	49.12	3.95	3.53
7	1.48	70.06	5.29	3.83
9	1.56	77.38	5.45	3.56
10.5	1.59	80.62	5.71	3.19

And putting sufficient particles close to the exit can help in resolving velocity at the vortex core.

After the incident shock diffracts at the exit of tube, the fluid behind it expands to form a slipstream line. Then, the slipstream rolls up to form a CVR behind the incident shock. In general, the evolution of CVR is basically classified into three stages, namely rapid growth, pinch-off, and free traveling stages (Murugan and Das 2010). As shown in Fig. 4a, a small vortex core can be seen faintly from the flow visualization and indicates the initial formation of CVR. Then, the CVR grows rapidly in size and moves downstream. At $t = 0.52$ ms, a trailing jet appears behind the leading CVR and interacts with the leading CVR. From the flow visualization in Fig. 4a–c, it can be observed that the core of CVR is stable and spherical, indicating that this CVR represents a laminar vortex. As the leading CVR grows, the trailing jet forms tiny shear layer vortices due to the Kelvin–Helmholtz-type instability shown in Fig. 4e, f. In this case, the trailing vortex is not merged into the leading CVR. The comparison between Fig. 4e and f shows that the size of the leading CVR almost no longer increases and instead exhibits the mechanism of vortex pinch-off. The phenomenon of vortex pinch-off was firstly observed by Gharib et al. (1998) in the formation of ICVRs. In the following subsection, we further analyze the pinch-off of the CVR. After the pinch-off of CVR, the physical separation between the leading CVR and the trailing vortices is observed, as shown in Fig. 4f. Subsequently, the CVR propagates downstream freely.

In order to investigate the compressibility effects on CVRs, the flow patterns of CVRs for PR = 3.5, 5, 7, 9, and 10.5 are presented in Fig. 5. These CVRs nearly travel at the same position of $X \approx 2D_t$ from the exit plane of shock tube.

As PR increases, M_s increases and velocity behind the incident shock also increases. As a result, the Reynolds number (Re_j) of the flow behind the incident shock increases as well. Re_j is defined as $Re_j = u_{max}D_t/\upsilon$, where u_{max} is the maximal velocity of the jet behind the incident shock and υ is the dynamic viscosity. For the flow with PR = 3, 5, 7, 9, and 10.5, the corresponding Reynolds number is 7.52×10^5, 10.65×10^5, 13.42×10^5, 13.70×10^5, and 13.98×10^5. The intuitive observation of Fig. 5 demonstrates that more total circulation and more trailing vortices are generated as M_s increases. From the flow visualization, it is observed that the CVRs for PR = 3 and PR = 5 have a stable and laminar vortex core, whereas the vortex cores of these CVRs for PR = 7, 9, and 10.5 are deformed and axially stretched into an oval core owing to the strong trailing jet, flow development, and the occurrence of embedded shock. As M_s further increases, the strength of embedded shock is enhanced and the axial

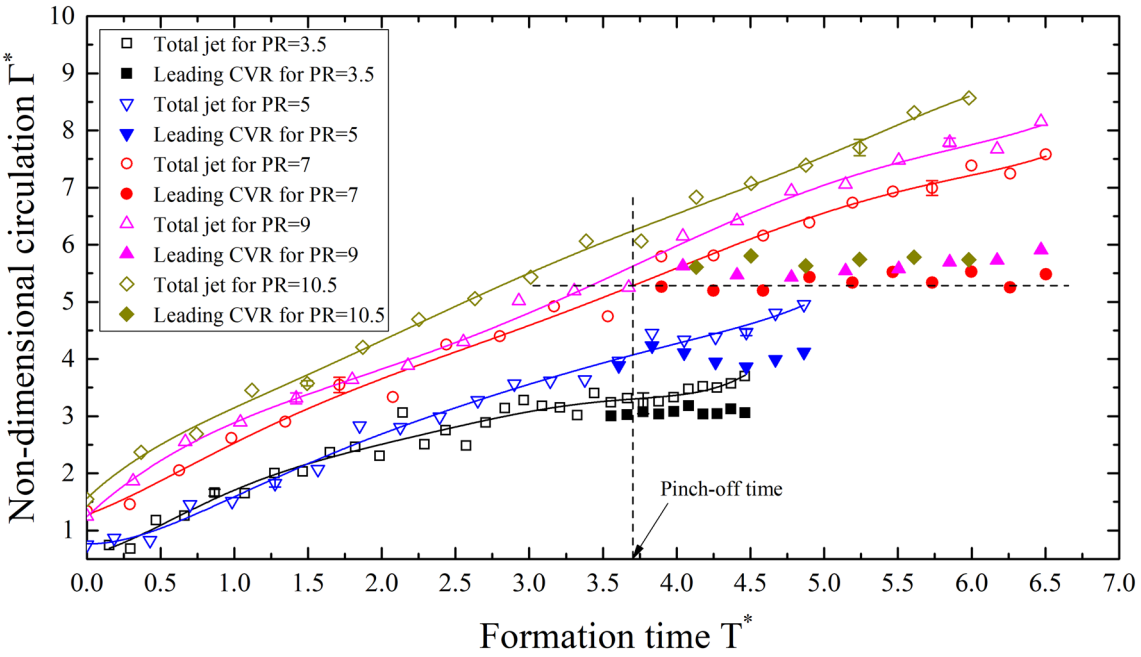

Fig. 8 Normalized circulation of the total jet and the leading CVR as a function of formation time for the five cases

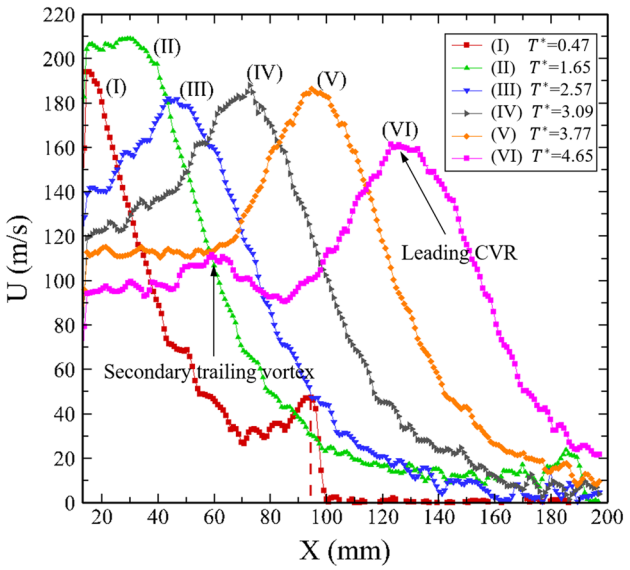

Fig. 9 The axial velocity profiles at the centerline of the shock tube at different times for the case of PR = 3.5 with M_s= 1.28 corresponding to the images shown in Fig. 4

stretch of vortex core is thereupon enhanced. When PR is larger than 7, the vortex core is already unstable and even become turbulent. The instability and turbulence of vortex core are closely related to many factors including but not limited to the compressibility effects and Reynolds number. As shown in Fig. 5c, d, the formation of CRVRs is observed for the case of PR = 9 and 10.5 with M_s= 1.56 and 1.59, which is smaller than the lowest M_s= 1.75 for the appearance of CRVRs observed by Murugan and Das (2010). However, the formation of CRVRs depends on not only the M_s, but also the length of driver section, both of which determine the amount of amplitude and the pulse duration. Small CRVR is due to weak trailing jet produced in the short driver section as compared to them where driver and driven section lengths were 165 mm and 1200 mm, respectively. The formation of single or multiple CRVRs depends on the value of impulse. And the interaction of trailing jet vortices entering the core of primary vortex ring could also form the CRVR.

3.2 Circulation evolution and Pinch-off of CVRs

In general, the circulation of a vortex can be calculated by integrating the vorticity with the vortex area or integrating the velocity along a path enclosing the vortex area. Because the error of velocity measurements is less than that of vorticity measurements, the circulation in our study is calculated by integrating the velocity along a path. Thus, the circulation of total jet and the leading CVR are calculated by,

$$\Gamma_{\text{total}} = \int_{s} \omega \mathrm{d}_s = \oint_{c} (u\mathrm{d}_x + v\mathrm{d}_y) \tag{2}$$

and

$$\Gamma_{\text{ring}} = \int_{s'} \omega \mathrm{d}_s = \oint_{c'} (u\mathrm{d}_x + v\mathrm{d}_y) \tag{3}$$

where s and s' indicate the areas of total jet and leading CVRs enclosed by $c(ABCDA)$ and $c'(A'B'C'D'A')$, respectively, as shown in Fig. 6. It should be noted that the circulation of the leading CVRs is calculated just when they can be distinguished from the trailing vortices.

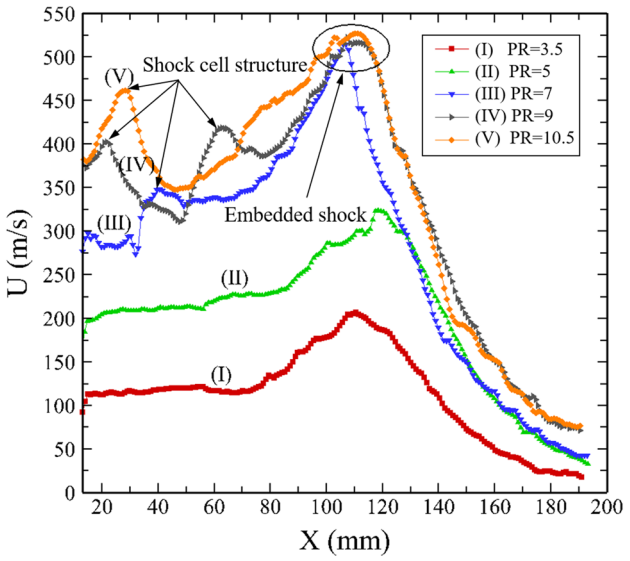

Fig. 10 The axial velocity profiles at the centerline of the shock tube for the five cases corresponding to the images shown in Fig. 5

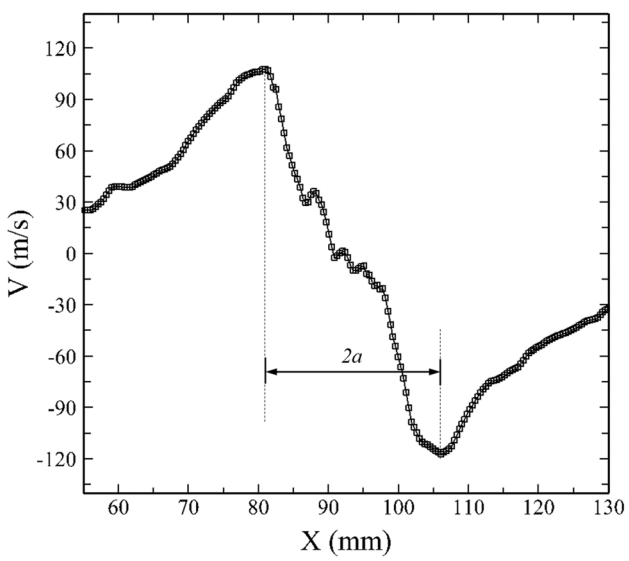

Fig. 11 The profile of the radial velocity at the position of the center ($Y = Y_{\text{core}}$) of vortex core for PR = 3.5 at t = 1.17 ms

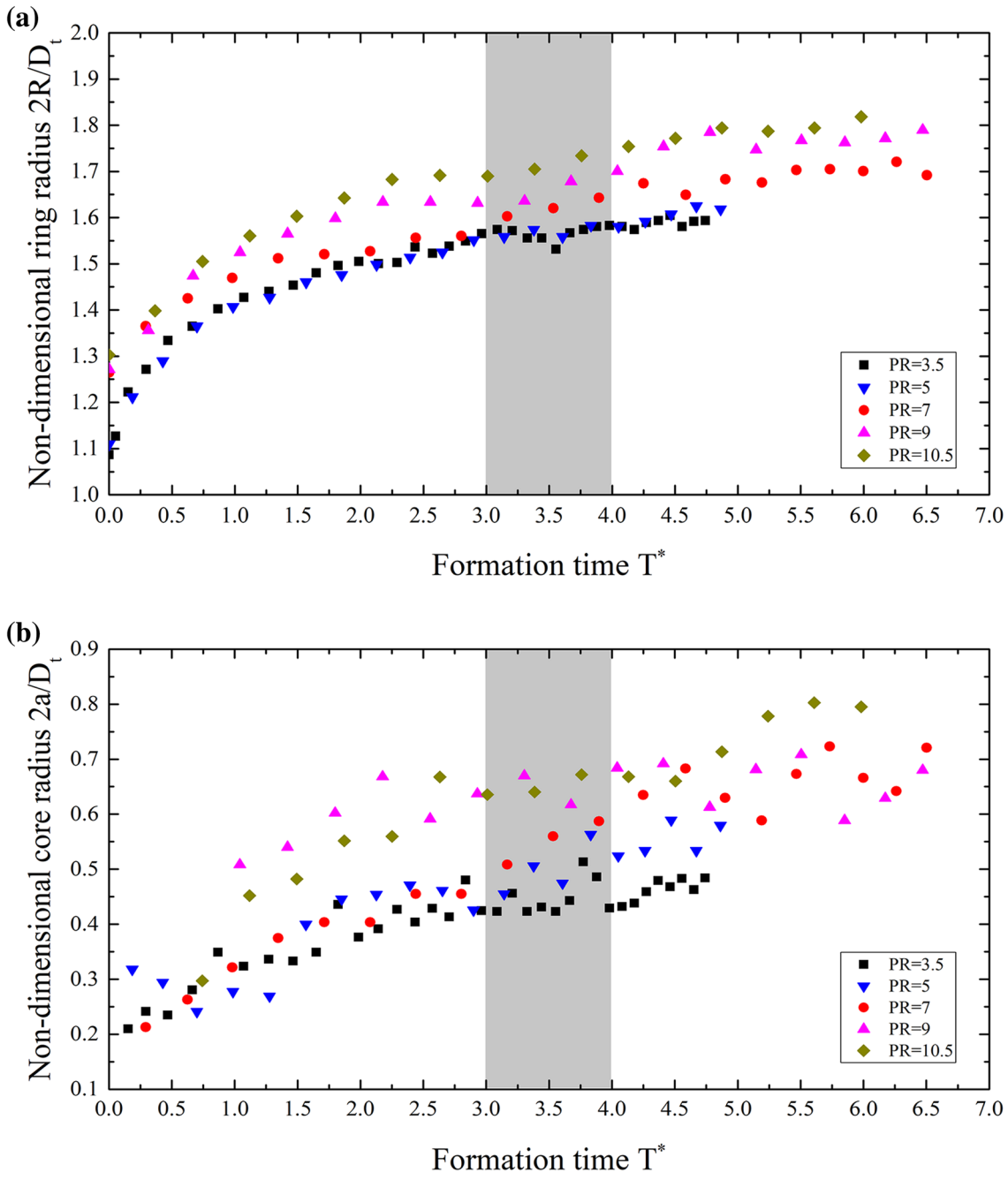

Fig. 12 The variations of vortex ring radius and vortex core radius with the formation time for the five cases. The shadow region indicates the varying range of the formation number: $F^*= 3.5 \pm 0.5$

Applying Eqs. (2) and (3), the circulation evolution of the total jet and the leading CVRs for all the five cases can be obtained. The circulation is normalized by the shock wave propagation velocity (U_s) in tube and the inner diameter of tube D_t. The expression of non-dimensional circulation is $\Gamma^* = \Gamma/(\frac{1}{2}U_s D_t)$. Based on the idea of vortex formation time for ICVRs, proposed by Gharib et al. (1998) the formation time T^* for CVRs is defined as $T^* = (\int_0^t u_j(t)\mathrm{d}_t/D_t)$, where $\int_0^t u_j(t)\mathrm{d}_t$ indicates the jet length and $u_j(t)$ is the time-dependent jet velocity at the exit plane of shock tube. According to the PIV measurements, the variation of $u_j(t)$ is presented in Fig. 7. It is found that the jet is accelerated at initial time and then slowly decays. As M_s increases, the maximal jet velocity increases. However, the maximal jet

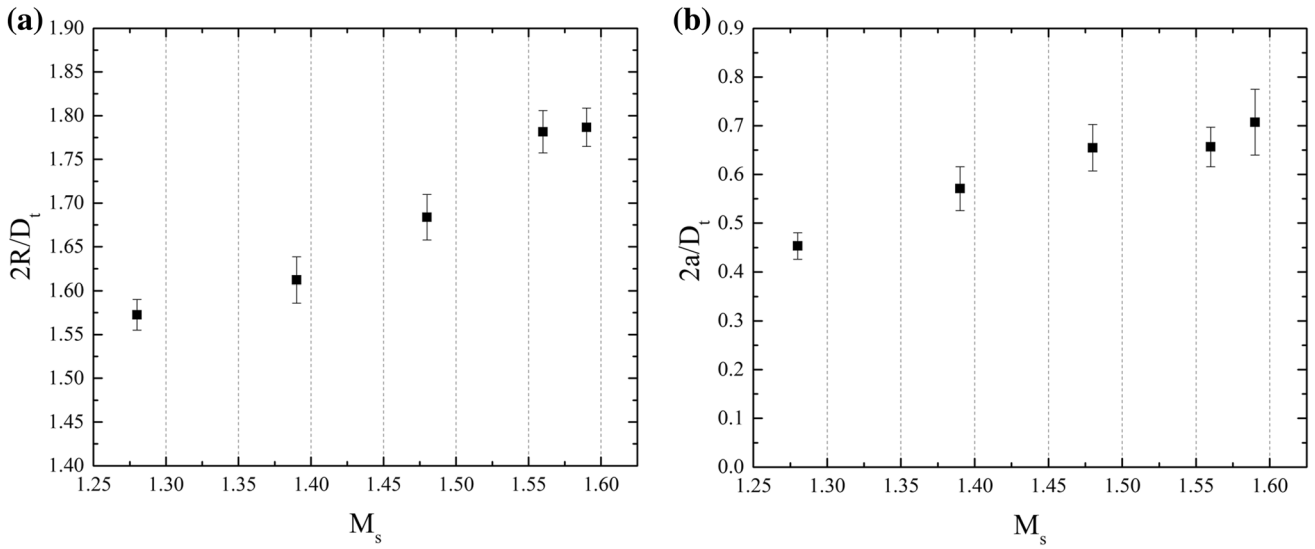

Fig. 13 The variations of the vortex ring radius and vortex core radius with the strength of the incident shock wave

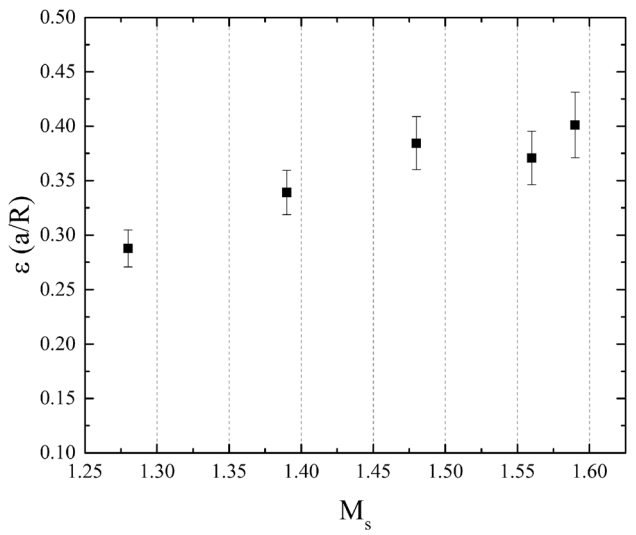

Fig. 14 The variations of the non-dimensional mean core radius ε with the Mach number of shock wave

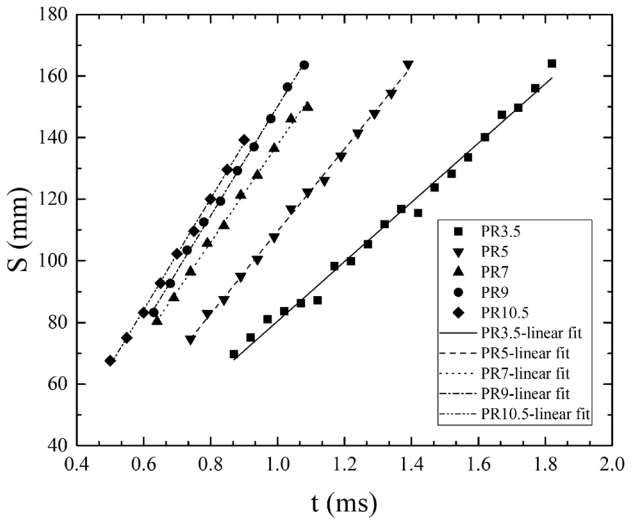

Fig. 15 The linear relationship between CVR propagating distance and time for the five cases

velocity for PR = 9 and 10.5 does not further increase significantly compared with that for PR = 7.

As shown in Fig. 8, the variation of both total circulation and leading CVR circulation (Γ^*) against with formation time (T^*) is presented. In Fig. 8, the circulation of total jet and the leading CVR is shown by solid lines with open symbols and solid symbols, respectively. It can be seen that the increase in total circulation exhibits a linear relationship with the formation time. According to the criterion proposed by Gharib et al. (1998), the onset of vortex pinch-off, termed as formation number (denoted by F^*), coincides with the time when the total circulation is equal to the final circulation of the leading CVR. Applying this criterion, the case of PR = 7 is taken as an example to determine the formation number, which is approximately 3.8. Subsequently, the formation number for each case in the present study is shown in Table 2.

In Table 2, the circulation and non-dimensional circulation of the leading CVR are shown, as well as the formation number. Taking the case of PR = 3.5 with M_s= 1.28 for example, the pinch-off process of the CVR is analyzed. In Fig. 4, the instantaneous formation time is T^* = 0.47, T^*= 1.65, T^*= 2.57, T^*= 3.08, T^*= 3.77, and T^*= 4.65 corresponding to t = 0.22 ms, t = 0.52 ms, t = 0.82 ms, t = 1.02 ms, t = 1.32 ms, and t = 1.77 ms. For this case,

the formation number is 3.2. Thus, it can be found that the size of the leading CVR grows before formation number, as shown in Fig. 4a–d. Once the vortex ring is pinched off, as shown in Fig. 4e, f, its size no longer grows. The additional circulation in the trailing jet forms the secondary trailing vortices. When T^*= 4.65, a physical separation between the leading CVR and the trailing vortices is observed. As shown in Table 2, the formation numbers of CVRs for different M_s are slightly varied but stay in the narrow range of 3.0–4.0, which agrees with that of ICVRs generated by the piston-cylinder apparatus. Table 2 shows that the formation number of CVRs for PR = 9 and PR = 10.5 is a little smaller than that for PR = 7. According to the investigations on ICVRs, the formation number may vary by some factors, including but not limited to the Reynolds numbers (Gao and Yu 2012), and velocity history of the jet at the nozzle exit (Shusser et al. 2006; Xiang et al. 2018b), whereas the compressibility effects should also have an important role on the formation number of CVRs. However, one cannot draw the robust conclusion that the formation number of CVRs shares a universal timescale that satisfies the optimal vortex formation principle proposed by Dabiri (2009). In the future works, we will further investigate the formation number of CVRs for more flow conditions and explain the mechanism of CVR pinch-off.

3.3 Axial velocity profiles at the centerline

For CVRs, the maximal velocity is the axial velocity near the centerline. According to the axial velocity, Baird (1987) classified the CVRs into subsonic and supersonic CVRs. CVRs are supersonic in the sense that the maximal axial velocity is supersonic in the frame of reference of the vortex ring. In addition, supersonic CVRs are usually associated with the existence of embedded shocks and therefore are also the CVRs with embedded shocks and the CVRs with CRVRs. Thus, the subsonic CVRs are also the shock-free CVRs. To reflect the vortex/wave interaction, the axial velocity profiles along the centerline of shock tube at different times for the case of PR = 3.5 are presented in Fig. 9. From the axial velocity profile at $T^* = 0.47$, one can observe the position of the incident shock, denoted by the dash line, is $X = 95$ mm from the exit plane of shock tube. In Fig. 9, the position of maximal axial velocity indicates the core position of the leading CVR. At T^*= 3.77, when the leading CVR is pinched off, the trailing jet can be seen clearly behind the leading CVR, as shown in Fig. 9. Moreover, a secondary peak of the axial velocity appears at T^*= 4.65 and indicates the rolling-up of a secondary vortex.

Owing to the enhancement of compressibility, CVRs will become supersonic. Figure 10 shows the centerline axial velocity profiles for the five cases with different *PRs*. When PR = 3.5 and 5, the corresponding Mach number of the incident shock is 1.28 and 1.39, for which the CVRs are shock-free and subsonic. When PR = 7, 9, and 10.5, an embedded shock appears inside the CVR, and a shock cell structure appears in the subsequent trailing jet as well.

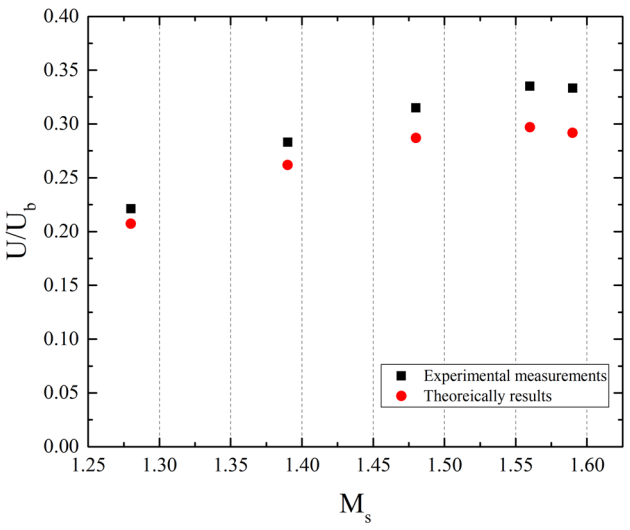

Fig. 16 The variation of CVR propagation velocities against M_s. The propagation velocities were obtained by our experimental measurements and theoretical equations (6)–(7), respectively

3.4 Vortex radius, core size, and vorticity distributions of CVRs

Core characteristics including the radius of vortex core (denoted by a) and the radius of vortex ring (denoted by R) are of particular importance to describe the dynamics of vortex rings. For ICVRs, the Fraenkel's second-order formula, the modified formula proposed by Sullivan et al. (2008), and the generalized model proposed by Kaplanski et al. (2009) are strongly dependent on the core characteristics. In general, the radius of vortex ring is defined as the distance between the center of the vortex core and centerline of the vortex ring. Figure 11 displays the profile of the radial velocity at $Y = Y_{\text{core}}$, where Y_{core} represents the position of the center of the vortex core. The coordinates $(X_{\text{core}}, Y_{\text{core}})$ of vortex core are defined by,

$$X_{\text{core}} = \frac{\int_{s'} \omega x \mathrm{d}_s}{\Gamma} \tag{4}$$

$$Y_{\text{core}} = \frac{\int_{s'} \omega y \mathrm{d}_s}{\Gamma} \tag{5}$$

where s' denotes the area of the leading CVR. Accordingly, the distance $2a$ along the X-axis between the maximum and minimum points at the ends of the approximately linear segment of the curve is set as the diameter of the vortex core.

In Fig. 12, the variations of the vortex ring radius and vortex core radius against the formation time are shown for the five cases. As the formation time proceeds, vortex ring radius and vortex core radius increase. Once the CVRs pinch off at F^*= 3.5±0.5, the vortex ring radius nearly remains unchanged, as shown in Fig. 12a. For the vortex core radius, it shares the similar tendency with the vortex radius before CVRs pinch off. However, the vortex core radii seem to continue to grow after the pinch-off of CVRs. This is largely because of the vorticity dissipation along the radial direction. In addition, compared with the subsonic CVRs for PR = 3.5 and 5, the vortex core radii of supersonic CVRs for PR = 7, 9, and 10.5 exhibit more fluctuation which are mainly due to the penetration of shear layer vortices into the primary vortex ring and their interaction with embedded shock.

After the occurrence of vortex pinch-off, CVRs begin to propagate downstream without growth. Then, one can detect the average values of vortex ring radius and vortex core radius of CVRs with error bars after T^*= 4.0, and their variations against the strength of the incident shock are shown in Fig. 13. It is found that both the vortex ring radii and the core radii increase with M_s when $M_s < 1.48$, whereas the two radii are likely limited when $M_s > 1.48$ because of the appearance of embedded shock. Generally, the non-dimensional mean core radius $\varepsilon(\varepsilon = a/R)$ is used to describe the core model of vortex rings. Figure 14 shows the variation of ε against M_s. It is found that the non-dimensional mean core radius ε is smaller than 0.4 in the present study, therefore indicting the CVRs belong to the thin-core vortex rings. In particular, the appearance of embedded shock significantly affects the vortex core by stretching the core shape and limiting the core size.

3.5 Propagation velocity of CVRs

Owing to the self-induction, vortex rings can propagate downstream with the self-induced velocity. Though massive investigations and modifications, the formulas for estimating the propagation velocity of ICVRs are more and more precise (Shaffman 1970; Shusser and Gharib 2000; Sullivan et al. 2008). As shown in the above investigations, compressibility significantly affects the core characteristics of CVRs and therefore affects the propagation velocity of CVRs.

The present study focuses on the propagation velocity (denoted by U) of the free traveling CVRs. As shown in Fig. 15, the axial position of vortex core of CVRs as a function of time after the occurrence of vortex pinch-off is presented. It is found that the displacement of CVRs has a strong linear relationship with time, indicating that the propagation velocity of CVRs almost keeps constant during the free traveling process and velocity decay due to energy dissipation is quite slight. Thus, by linear fitting, the propagation velocity of CVRs for M_s= 1.28, 1.39, 1.48, 1.56, and 1.59 is 96.3 m/s, 133.7 m/s, 158.5 m/s, 177.7 m/s, and 180.1 m/s, respectively. It should be mentioned that the velocity here is the averaged velocity of the CVR after the occurrence of CVR pinch-off.

By considering the compressibility effects, a formula was proposed by Moore (1985) to estimate the propagation velocity of an inviscid CVR. The formula is expressed by

$$U = \frac{\Gamma_r}{4\pi R}\left[\ln\frac{8}{\varepsilon} - \frac{1}{4} - \frac{5}{12}M_c^2 + O(M_c^4)\right] \tag{6}$$

where Γ_r is the CVR circulation and M_c is the Mach number of vortex core defined by

$$M_c = \frac{\Gamma_r}{2\pi a c_\infty} \tag{7}$$

where c_∞ is the sound speed at the far field.

Figure 16 presents the CVR propagation velocities obtained by our experimental measurements and the theoretical calculations based on Eqs. (6)–(7), respectively. The propagation velocity is approximately 0.2–0.4U_s, where U_s is the propagation velocity of the incident shock in the shock tube. Both the experimental and theoretical results show that the propagation velocity performs an increased tendency with M_s when $M_s < 1.56$. For M_s= 1.56 and M_s = 1.59, the increase in the vortex ring velocity is slower than the increase in the shock velocity. Therefore, compared to $M_s = 1.56$, the non-dimensional velocity (U/U_s) is slightly smaller for $M_s = 1.59$. And this may be due to the appearance of embedded shock in the CVRs that significantly affects the propagation velocity of CVRs. The peak propagation velocity of $W = 0.35U_s$ is demonstrated. In addition, the experimental values are slightly larger than the theoretical results and the differences between them become more apparent when M_s is larger than 1.48. Such differences are probably attributed to the following factors: (1) the assumption of inviscid fluids and perfect core model in Eq. (6), (2) the errors in the estimation of a and R, and (3) theoretical equations ignoring the effects of embedded shock when $M_s > 1.48$.

4 Conclusions

In this paper, the formation and dynamics of compressible vortex rings (CVRs) generated by a shock tube were experimentally investigated using PIV technique. To investigate the compressibility effects on the formation and dynamics of CVRs, the pressure ratio between driver section and driven section (PR) was varied from 3.5 to 10.5. Correspondingly, the Mach number of the incident shock (M_s) was varied from 1.28 to 1.59 and three typical CVRs are generated including

shock-free CVRs, CVRs with embedded shock, and CVRs with embedded shock and CRVRs.

It is observed that a laminar CVR begins to roll up and grows in size until the occurrence of vortex pinch-off after the incident shock leaves the exit of shock tube for PR = 3.5 with M_s= 1.28. As M_s increases from 1.28 to 1.59, the vortex core of CVRs deforms and even becomes turbulent for $M_s \geq 1.48$ and the counter-rotating vortex rings (CRVRs) appear for $M_s \geq 1.56$. The deformation of vortex core is related to many factors including the embedded shock, shear layer trailing vortices, and the vortex induced shock. By referring to the idea of vortex formation time, CVRs are found to pinch off at the formation number within the narrow range of $F^* = 3.5 \pm 0.5$ for the range of PR = 3.5–10.5 with DL = 100 mm in the present study. In addition, the formation number of CVRs basically agrees with that of the ICVRs generated by the piston-cylinder apparatus and satisfies the principle of optimal vortex formation number.

To investigate the compressibility effects on the dynamics of CVRs, the axial velocity profiles, vortex core characteristics, and the propagation velocity of CVRs were analyzed in this paper. It is found that the maximal axial velocity is larger than the speed of sound when $M_s \geq 1.48$, therefore resulting in the appearance of the embedded shock and indicting these CVRs are supersonic. The tendency of vortex radii (R) and core radii (a) with M_s shows that the embedded shock has limited the core growth by axially stretching the core shape. In addition, the non-dimensional mean core radius $\varepsilon(\varepsilon=a/R)$ of CVRs is lower than 0.4, thereby suggesting that the CVRs belong to the thin-core vortex rings. By the experimental measurements, we obtained the propagation velocity of free traveling CVRs, which shows basic agreement with that estimated by the theoretical formula proposed by Moore (1985). Moreover, it is found that the propagation velocity of CVRs seems to arrive the peak velocity of $U = 0.35U_s$ owing to the appearance of embedded shock.

These observations in this paper not only provide insights into the formation of CVRs, but also demonstrate the compressibility effects on the dynamics of CVRs. This information is useful to understand the formation and dynamics of both CVRs and other compressible vortices. In the further, we would like to further investigate the formation of CVRs with more conditions to obtain more robust conclusions particularly including the formation number of CVRs. In addition, more precise dynamic models for CVRs are worth studying.

Acknowledgements Financial support from the State Key Development Program of Basic Research of China (No. 2014CB744802) is gratefully acknowledged. This work was also supported by the NSFC Project (Nos. 91441205, 91941301) and China Postdoctoral Science Foundation (No. 2018M642007).

References

Arakeri J, Das D, Krothapalli A, Lourenco L (2004) Vortex ring formation at the open end of a shock tube: a particle image velocimetry study. Phys Fluids 16:1008–1019

Aydemir E, Worth N, Dawson J (2012) The formation of vortex rings in a strongly forced round jet. Exp Fluids 52:729–742

Baird J (1987) Supersonic vortex rings. Proc R Soc Lond A 409:59–65

Brouillette M, Hebert C (1997) Propagation and interaction of shock-generated vortices. Fluid Dyn Res 21:159–169

Brown S (1965) The compressible inviscid leading-edge vortex. J Fluid Mech 22:17–32

Chandra N, Ganpule S, Kleinschmit N, Feng R, Holmberg A, Sundaramurthy A, Selvan V, Alai A (2012) Evolution of blast wave profiles in simulated air blasts: experiment and computational modeling. Shock Waves 22:403–415

Dabiri J (2009) Optimal vortex formation as a unifying principle in biological propulsion. Annu Rev Fluid Mech 41:17–33

Didden N (1979) On the formation of vortex rings: rolling-up and production of circulation. J Appl Mech Phys 530:101–116

Dora CL, Murugan T, De S, Das D (2014) Role of slipstream instability in formation of counter-rotating vortex rings ahead of a compressible vortex ring. J Fluid Mech 753:29–48

Elder F, Haas D (1952) Experimental study of the formation of a vortex ring at the open end of a cylindrical shock tube. J Appl Phys 23:1065–1069

Fraenkel L (1972) Examples of steady vortex rings of small cross-section in an ideal fluid. J Fluid Mech 51:119–135

Gao L, Yu S (2010) A model for the pinch-off process of the leading vortex ring in a starting jet. J Fluid Mech 656:205–222

Gao L, Yu S (2012) Development of the trailing shear layer in a starting jet during pinch-off. J Fluid Mech 700:382–405

Gharib M, Rambod E, Shariff K (1998) A universal time scale for vortex ring formation. J Fluid Mech 360:121–140

Ishii R, Fujimoto H, Hatta N, Umeda Y (1999) Experimental and numerical analysis of circular pulse jets. J Fluid Mech 392:129–153

Kaplanski F, Sazhin S, Fukumoto Y, Begg S, Heikal M (2009) Examples of steady vortex rings of small cross-section in an ideal fluid. J Fluid Mech 622:233–258

Kontis K, An R, Edwards J (2006) Compressible vortex-ring interaction studies with a number of generic body configurations. AIAA J 44:2962–2978

Krueger P (2005) An over-pressure correction to the slug model for vortex ring circulation. J Fluid Mech 545:427–443

Minota T (1997) Dynamic motion of a compressible vortex ring. Proc SPIE Int Soc Opt Eng 3173:241–248

Moore D (1985) The effect of compressibility on the speed of propagation of a vortex ring. Proc R Soc Lond A 397:87–97

Moore D, Pullin D (1987) The compressible vortex pair. J Fluid Mech 187:171–204

Murugan T, Das D (2007) Structure and acoustic characteristics of supersonic vortex ring. In: 9th international symposium on fluid control, measurement and visualization, pp 16–21

Murugan T, Das D (2010) Characteristics of counter-rotating vortex rings formed ahead of a compressible vortex ring. Exp Fluids 49:1247–1261

Murugan T, Das D (2018) Numerical study of blast wave generation through shock tube and its comparison with free-field blast wave parameters. In: 5th national symposium on shock waves, pp 26–28

Murugan T, De S, Dora C, Das D (2012) Numerical simulation and PIV study of compressible vortex ring evolution. Shock Waves 22:69–83

Murugan T, De S, Dora C, Das D, Kumar P (2013) A study of the counter rotating vortex rings interacting with the primary vortex ring in shock tube generated flows. Fluid Dyn Res 45:025506

Payman W, Shepherd W (1946) Explosion waves and shock waves; the disturbance produced by bursting diaphragms with compressed air. Proc R Soc Lond A 186:293–321

Phan K, Stollery J (1983) The effect of suppressors and muzzle brakes on shock wave strength. In: Proceedings of the 14th international symposium on shock tubes and waves Springer, Berlin, pp 123–129

Shaffman P (1970) The velocity of viscous vortex rings. Stud Appl Maths 49:371–380

Shariff K (1992) Vortex rings. Annu Rev Fluid Mech 24:235–279

Shusser M, Gharib M (2000) Energy and velocity of a forming vortex ring. Phys Fluids 12:618–621

Shusser M, Rosenfeld M, Dabiri J, Gharib M (2006) Effect of time-dependent piston velocity program on vortex ring formation in a piston/cylinder arrangement. Phys Fluids 18:033601

Sullivan I, Niemela J, Hershberger R, Bolster D, Donnelly R (2008) Dynamics of thin vortex rings. J Fluid Mech 609:319–347

Vieille P (1899) Deformation des ondes au cours de leur propagation. Comptes Rendus Hebdomadaires des Seances de l Academie des Sciences 128:1437–1440

Xiang Y, Liu H, Qin S (2018a) A unified energy feature of vortex rings for identifying the pinch-off mechanism. ASME J Fluids Eng 140:011203

Xiang Y, Qin S, Liu H (2018b) Patterns for efficient propulsion during the energy evolution of vortex rings. Eur J Mech B Fluid 71:47–58

Zare-Behtash H, Gongora O, Kontis K (2009) Global visualization and quantification of compressible vortex loops. J Vis 12:233–240